Unrestricted molecular motions enable mild photothermy for recurrence-resistant FLASH antitumor radiotherapy

Hanchen Shen [a,b,1], Hongbin Wang [c,1], Jianlan Mo [d,1], Jianyu Zhang [b], Changhuo Xu [e], Feiyi Sun [b], Xinwen Ou [b], Xinyan Zhu [b], Lidong Du [b,e], Huaqiang Ju [b], Ruquan Ye [f], Guangfu Shi [g], Ryan T.K. Kwok [b], Jacky W.Y. Lam [b], Jianwei Sun [b], Tianfu Zhang [a,***], Shipeng Ning [g,**], Ben Zhong Tang [b,h,*]

[a] Affiliated Cancer Hospital & Institute of Guangzhou Medical University, School of Biomedical Engineering, Guangzhou Medical University, Guangzhou, China
[b] Department of Chemistry, Hong Kong Branch of Chinese National Engineering Research Center for Tissue Restoration and Reconstruction, Division of Life Science, and State Key Laboratory of Molecular Neuroscience, The Hong Kong University of Science and Technology, Kowloon, Hong Kong, China
[c] The Second Ward of Breast Surgery, Cancer Hospital Affiliated to Harbin Medical University, Heilongjiang, 150081, China
[d] Department of Anesthesiology, Maternal and Child Health Hospital of Guangxi Zhuang Autonomous Region, Nanning, China
[e] MOE Frontiers Science Center for Precision Oncology, Faculty of Health Sciences, University of Macau, Macao, China
[f] Department of Chemistry, State Key Laboratory of Marine Pollution, City University of Hong Kong, Hong Kong, China
[g] Department of Breast Surgery, The Second Affiliated Hospital of Guangxi Medical University, Nanning, China
[h] School of Science and Engineering, Shenzhen Institute of Aggregate Science and Technology, The Chinese University of Hong Kong, Shenzhen (CUHK-Shenzhen), Guangdong, 518172, China

ARTICLE INFO

ABSTRACT

Ultrahigh dose-rate (FLASH) radiotherapy is an emerging technology with excellent therapeutic effects and low biological toxicity. However, tumor recurrence largely impede the effectiveness of FLASH therapy. Overcoming tumor recurrence is crucial for practical FLASH applications. Here, we prepared an agarose-based thermo-sensitive hydrogel containing a mild photothermal agent (TPE-BBT) and a glutaminase inhibitor (CB-839). Within nanoparticles, TPE-BBT exhibits aggregation-induced emission peaked at 900 nm, while the unrestricted molecular motions endow TPE-BBT with a mild photothermy generation ability. The balanced photothermal effect and photoluminescence are ideal for phototheranostics. Upon 660-nm laser irradiation, the temperature-rising effect softens and hydrolyzes the hydrogel to release TPE-BBT and CB-839 into the tumor site for concurrent mild photothermal therapy and chemotherapy, jointly inhibiting homologous recombination repair of DNA. The enhanced FLASH radiotherapy efficiently kills the tumor tissue without recurrence and obvious systematic toxicity. This work deciphers the unrestricted molecular motions in bright organic fluorophores as a source of photothermy, and provides novel recurrence-resistant radiotherapy without adverse side effects.

1. Introduction

Radiotherapy is one of the most widely used conventional therapeutic strategies for cancer patients [1]. DNA double-strand breaks induced by ionizing radiation are one of the main mechanisms of its antitumor effect [2]. However, the serious side effects on the human body are a major concern in radiotherapy [3]. Clinical researchers have developed modern radiotherapy technologies to improve therapeutic outcomes, including helical tomotherapy and proton beam therapy [3, 4]. Among these emerging technologies, ultrahigh dose-rate ($\geq$40 Gy/s) (FLASH) radiotherapy is thought to be a significant technological breakthrough, because it can minimize radiation-induced adverse

effects while suppressing the tumor growth as effectively as the conventional dose-rate (0.01–0.40 Gy/s) irradiation [5,6]. The FLASH effect protects normal tissues by reducing the oxygen content and activating metabolic pathways, while the tumor and normal cells have different radiobiological processes to lead to a different susceptibility to FLASH therapy [5,7–9].

Unfortunately, cancer cells can repair and adapt to the changes induced by radiotherapy [10–12]. This fact significantly impede the therapeutic effects of FLASH radiotherapy and result in tumor recurrence. Successfully addressing tumor recurrence is essential for the practical usage of FLASH technology. Cancer cells can recover from radiation injuries through cellular DNA damage responses (DDRs). The DNA repair capacity is a critical DDR that affects how cells respond to radiation. Therefore, inhibiting DNA repair could be a promising therapeutic approach to overcome the tumor radioresistance and recurrence [13–15]. Glutamine metabolism is closely related to DNA repair [16]. Glutaminase (GLS) is a key enzyme involved in glutamine metabolism that allows the conversion of glutamine to glutamate [17]. As a first-in-class GLS inhibitor, CB-839 can disturb glutamine metabolism and further influence the DNA repair through mechanisms including increased reactive oxygen species (ROS) formation and glutamine deficiency effects [18–20]. The synergistic effect of using CB-839 in cancer therapy has been widely explored [21–23]. Therefore, combining CB-839 with FLASH would be an efficient and safe strategy. The effective delivery of small-molecule drugs is crucial for achieving satisfactory therapeutic effects and ensuring patient compliance. Localized injectable hydrogels have become increasingly popular in modern medicine due to their efficient delivery of therapeutic agents *in situ* and the sustained drug release [24]. Responsible hydrogel releases the peak amount of drug within the therapeutic window using appropriate stimuli, enhancing both the therapeutic effect and the patient compliance in cancer therapy [25]. Also, this strategy avoids the circulatory system and reduces the systematic toxicity to normal tissues.

Photothermal technology is promising in modern medicine and can be used in various fields such as smart drug delivery [26,27], antitumor therapy [28,29], infection treatment [30], and neural modulation [31–33]. Photothermal agents with strong absorption in the near-infrared window (NIR, 650–1700 nm) are attractive because they can be excited deeply inside the biological tissues [31,34]. Thus, NIR photothermal agents can control responsible hydrogel remotely and non-invasively to achieve smart drug delivery systems. On the other hand, in antitumor applications, the mechanism for photothermal therapy (PTT) is a local high temperature that induces cell death in tumor tissues [35]. To avoid nonspecific heat diffusion and potential immunosuppressive effects, researchers started performing PTT with mild hyperthermia with the highest temperature of about 45 °C [36]. Mild PTT (mPTT) can efficiently induce cell death and reduce side effects, improving vascular permeability and the delivery of antitumor agents and activating the immune system. Importantly, recent research indicates that mPTT disrupts DNA damage repair pathways, which could be highly valuable when combined with radiotherapy [37,38]. However, it is hard for photothermal agents to generate a long-lasting therapeutic effect, which is a prerequisite for recurrence-resistant therapy. Therefore, we speculate that a combination of FLASH, chemotherapy, and mPTT will enable an optimized drug delivery system, effectively suppress tumor recurrence, and simultaneously ensure the efficacy and biosafety.

Photothermal agents designed based on molecular motion-facilitated non-radiative decay (MMFND) have unique advantages such as simple design, stable performance, superior photostability, and bioenvironmental stability [39]. However, the molecular motion is always maximized to achieve strong photothermal effects, which often sacrifices the photoluminescence. Fluorescence (FL) imaging is essential in modern medicine by monitoring the physiological processes or exogenous materials, possessing the potential for dynamic visualization with advantages of great sensitivity, high resolution, and low cost [40]. How

to maximize the usage of absorbed energy to achieve an excellent photothermal effect (requiring molecular motions) and strong photoluminescence (inhibiting molecular motions) is still challenging.

From the literature, we are greatly magnetized by the unique photophysical properties of NIR-II fluorophores with FL emission in 1000–1700 nm [41]. However, the quantum yield (QY) of current NIR-II molecules is typically below 1% [42]. The low QY value indicates that much energy is dissipated through non-radiative transitions to lead to photothermy generation. Therefore, we hypothesize that even NIR-II fluorophores with high QYs are promising candidates for photothermal therapy. To confirm our hypothesis, we selected a luminogen called TPE-BBT to investigate its photothermal effect. TPE-BBT is a NIR-II fluorophore with a benzobisthiadiazole (BBT) core, exhibiting an aggregation-induced emission (AIE) peak at 900 nm. It has an ultrahigh QY of about 2% in nanoparticles [42]. We found that when forming aggregates, TPE-BBT still shows unrestricted molecular motions to provide non-radiative decay and a subsequently mild photothermal effect. Thus, based on TPE-BBT, we designed a NIR-laser (660 nm) controlled thermosensitive agarose hydrogel system named TCH for recurrence-resistant FLASH radiotherapy (Scheme 1). TCH was prepared by mixing TPE-BBT dots (TDs) and CB-839 liposomes (CLs) in a 60 °C agarose solution, which formed a gel on the tumor site when at body temperature. The strong FL of TPE-BBT enables material tracking for therapy and biosafety evaluation. NIR-laser irradiation controls the release of CB-839 and induces mPTT. Both chemotherapy and mPTT cause DNA damage and inhibit the homologous recombination (HR) repair pathways. Due to the synergistic effect, the FLASH radiotherapy demonstrates an excellent antitumor effect without tumor recurrence and obvious systematic toxicity. Thus, this work explores the usage of unrestricted molecular motions for designing phototheranostics agents and presents a promising recurrence-resistant FLASH strategy.

2. Materials and methods

2.1. Materials

CB-839 was purchased from Aladdin Co. Ltd. Low melting-point agarose was purchased from Yare Shanghai. Dil fluorescent dye was obtained from Solarbio Life Science. Cholesterol (Chol) and 1,2-dipalmitoyl-*sn*-glycero-3-phosphocholine (DPPC) were purchased from A.V.T (Shanghai, China). Compound **1** was purchased from Zhengzhou Ruke Biological Co., Ltd. Compound **2** (1-(4-phenylboronic acid pinacol ester)-1,2,2-triphenylethene) was purchased from Energy Chemical. All of the aqueous solutions were prepared using purified deionized (DI) water purified with a purification system (Direct-Q3, Millipore, USA). The other solvents used in this work were purchased from Sinopharm Chemical Reagent (China) and Aladdin-Reagent (China). All the chemical reagents were used without further purification.

2.2. Measurements

^{1}H and ^{13}C NMR spectra were measured on a Bruker AVIII 400 NMR spectrometer using CDCl$_3$ as a deuterated solvent and tetramethylsilane (TMS) as an internal reference. High-resolution mass spectra (HRMS) were recorded on a Water's Xevo G2-XS Tof mass spectrometer with an Electrospray source. UV–vis–NIR absorption spectra were measured using a UV–vis spectrophotometry Lambda 35 (PerkinElmer). Photoluminescence (PL) spectra were recorded on a Horiba Fluorolog-3 Spectrofluorometer. The diameter of nanoparticles was measured by dynamic light scattering (DLS, Nano-Zen 3600, Malvern Instruments, UK). Transmission electron microscopy (TEM) images were characterized by a JEOL JEM-2100 microscope at 200 kV (JEOL Ltd., Japan). Scanning electron microscope (SEM) images were captured on a Hitachi FE-SEM S4800 instrument with an acceleration voltage of 3 kV. Rheology experiments were performed on an Anton Paar rheometer. The photothermal images during laser irradiation were recorded using the
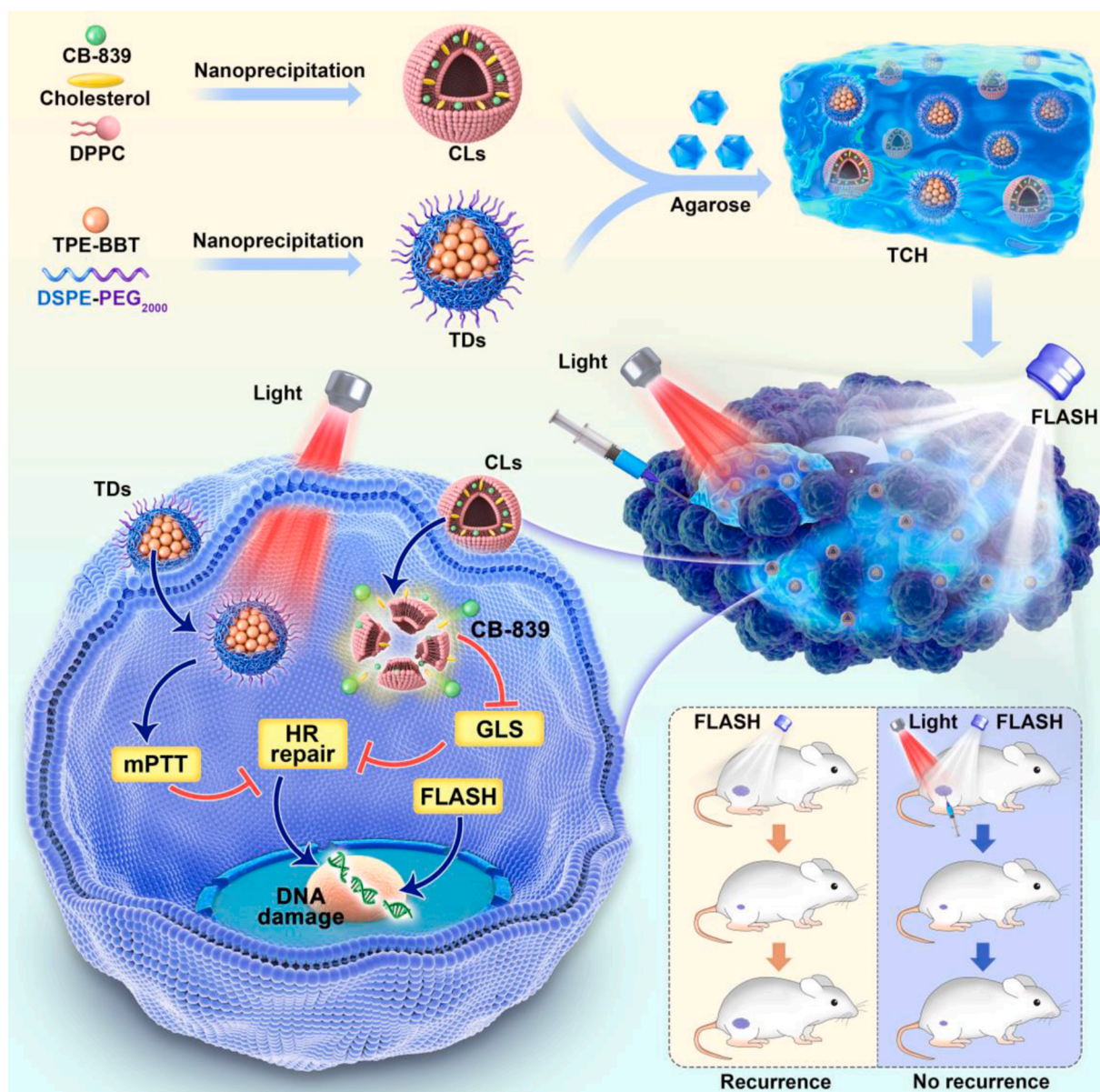
Scheme 1. Schematic illustration of the preparation and application of TPE-BBT dots (TDs) and CB-839 liposomes (CLs) co-loaded agarose thermosensitive hydrogel for recurrence-resistant tumor therapy. TCH: TDs and CLs co-loaded hydrogel; mPTT: mild photothermal therapy; HR repair: Homologous recombination repair; GLS: glutaminase; FLASH: ultrahigh dose-rate radiotherapy.

infrared thermal imaging system FOTRIC 225.

2.3. Theoretical calculations

All the compounds were fully optimized with the DFT method using M06-2X density functional [43] and 6-31G(d,p) basis set [44]. London-dispersion effects were also considered using Grimme's DFT-D3 correction [45] to further describe long-range inter/intramolecular interactions. Analytical frequency calculations were also performed at the same level of theory to confirm that the optimized structures were at a minimum point. Time-dependent density functional theory (TD-DFT) [46] was utilized at the same level of theory to calculate optimized excited (S_1) geometries and energy levels. For the crystalline phase of TPE-BBT, geometries and reorganization energy were calculated based on a combined quantum mechanics and molecular mechanics (QM/MM) model selected from the crystal packing structures. For the TPE-BBT aggregates, QM/MM model was selected from the molecular dynamics (MD) simulation. The MD simulation method was reported in our

previous work [42]. The equilibrated system showing the strongest intermolecular interactions (130.7 ns) was picked for further DFT calculation. The water molecules (hydrogen and oxygen atoms) within a radius of 5 Å around the simulated aggregate are retained to simulate the situation of an aqueous solution. The central molecule in the crystal structure, the innermost molecule in the simulated aggregate (embedded TPE-BBT), and a surface molecular in the simulated aggregate (exposed TPE-BBT) were treated as the QM part at (TD) M06-2X-D3/6-31G(d,p) level and the surrounding molecules were frozen and acted as the MM part with the universal force field (UFF). All the above quantum chemical calculations were carried out using Gaussian 16 program [47]. Reorganization energy analysis was performed using Molecular Materials Property Prediction Package (MOMAP) [48–50].

2.4. Preparation and characterization of AIE nanoparticles (TDs)

A mixture of TPE-BBT (1 mg), DSPE-PEG$_{2000}$ (1.5 mg), and THF (1

mL) was sonicated (12 W output) to obtain a clear solution. The mixture was quickly injected into 9 mL of water, which was sonicated vigorously in water for 2 min. The mixture was stirred in fume hood for 12 h to remove the THF. The solution was performed for ultrafiltration (molecule weight cut off 100 kDa) at 3000 g for 30 min to prepare the TDs. The concentration of TPE-BBT is 100 µg/mL, and the concentration can be tuned by ultrafiltration.

2.5. Preparation and characterization of CB-839 loaded liposomes (CLs)

A mixture of 27 mg DPPC, 2.8 mg Chol, and 5 mg CB-839 were dissolved in chloroform, and then evaporated at 55 °C for 80 min to form a thin film in a rotary evaporator. Then, the film was hydrated with PBS solution at 37 °C for 5 min and subjected to ultrasound followed by repeatedly extruding through 100 nm polycarbonate pores. The resultant particles were dialyzed overnight in a dialysis bag (MWCO 300 kDa) to remove unencapsulated CB-839. The loading capacity and release profile of CB-839 were calculated by UV–vis spectra. The concentration of CB-839 is 40 µg/mL.

2.6. Preparation and characterization of TDs and CL co-loaded hydrogel (TCH)

The general protocol for the hydrogel preparation is as follows. The prepared TDs (0.5 mg TPE-BBT) and CLs (0.2 mg CB-839) were added into 5 mL 2% low melting-point agarose solution. Cooling down the solution can form TCH for further use.

2.7. Photothermal ability of TCH

A 660 nm NIR-laser (Changchun New Industries Tech.Co., Ltd., Changchun, China) was used to stimulate the different concentrations of TCH in an aqueous medium under different power. The photothermal images of TDs or TCH during laser irradiation were recorded every 30 s using a Fotric 225 Thermal Camera.

2.8. Photothermal conversion efficiency

A 660 nm NIR-laser (Changchun New Industries Tech.Co., Ltd., Changchun, China) was used to stimulate the TDs (100 µg/mL TPE-BBT) in a PBS medium. The photothermal images of TDs during laser irradiation were recorded every 30 s using an infrared thermal imaging system. The photothermal conversion efficiency was calculated using the following equation [51]:

$$\eta = \frac{hS(T_{max} - T_{surr}) - Q_0}{I(1 - 10^{-A_\lambda})}$$

where h is the heat transfer coefficient, S is the surface of the container, T_{max} and T_{surr} are the equilibrium temperature and ambient temperature, respectively. Q_0 is the heat associated with the light absorbance of the solvent, A_λ is the absorbance of TDs at 660 nm, and I is the laser power density. According to the above equation, the η value of TDs was about 16.97%.

2.9. CB-839 release study

The *in vitro* CB-839 release profile from CL was carried out. 5 mL PBS containing CLs (0.2 mg CB-839) and TDs (0.5 mg TPE-BBT) were sealed into a dialysis bag with the molecular weight cutoff of 12 kDa. Then, the dialysis bag was immersed into 20 mL of release media with 0.1% Tween 20 and shaken at 150 rpm at a temperature of 37 °C. To investigate the stimuli effect of laser irradiation, the release experiment of CB-839 was performed with or without 1 W/cm² 660 nm laser irradiation for 3 min initially. At appropriate time points, the released CB-839 was measured by a UV–vis spectrophotometry. The *in vitro* CB-839 release profile from

TCH was also carried out. 5 mL TCH containing 0.2 mg CB-839 was added into the culture dish. The release experiment of CB-839 was performed with or without 1 W/cm² 660 nm laser irradiation for 3 min at appropriate time points. After the NIR irradiation, 100 µL of different samples were collected, and the CB-839 contents were measured by UV–vis spectra.

2.10. Parameters of FLASH radiotherapy

In our manuscript, FLASH radiotherapy was delivered using external beam radiation with electrons from the China Academy of Engineering Physics. The mean dose rate in the macro-pulse is 100 Gy/s. A macro-pulse consists of trains of numerous micro-pulses. These micro-pulses follow a quasi-Gaussian distribution with a period of 18.5 ns. Each micro-pulse is about 3 ps long (in rms). The instantaneous dose rate within the micro-pulse is 0.6 MGy/s, which is 6000 times the mean dose rate.

2.11. In vitro cancer cell internalization

HCT116 cells were seeded in 24-well plates and cultured for 12 h. Then, 100 µL of Dil ($\lambda_{ex} = 549$ nm, $\lambda_{em} = 565$ nm) labeled CLs (containing 40 µg/mL CB-839) was added to the medium. Then, the cells were incubated for 1 h or 4 h at 37 °C and 5% CO₂, and washed with PBS three times. The cells were harvested, stained with DAPI, and imaged using a fluorescence microscope (IX81, Olympus, Japan).

2.12. Western blot (WB) analysis in vitro

HCT116 cells (8×10^6 per plate) were incubated with 6 different groups: (1) PBS; (2) NIR (660 nm laser, 1W/cm², 5min); (3) TCH; (4) TH + NIR; (5) CLs; and (6) TCH + NIR. The CB-839 concentration was 40 µg/mL. After 12 h of incubation, the cells of each group were collected, the protein lysis solution was added to extract the total cell protein, and the protein was quantified according to the instructions of the BCA reagent. After electrophoresis, the separated proteins were transferred to PVDF membranes. After the film was transferred, the milk was used for blocking for 2 h, and the diluted primary anti-GLS antibody solution (diluted according to the recommended concentration of each antibody instruction) was added overnight. After washing, the secondary antibody was added, exposed, developed, and filmed.

2.13. Intracellular GSH detection and DNA damage repair assays

The commercially available GSH assay kit was used to detect the depletion of GSH. HCT116 cells were incubated with 5 different groups: (1) PBS; (2) NIR (660 nm laser, 1W/cm², 5min); (3) CLs; (4) TCH; and (5) TCH + NIR. The CB-839 concentration was 40 µg/mL. After 12 h of incubation, the GSH content was measured by employing a commercial colorimetric GSH assay kit. The assay was carried out according to the manufacturer's instructions. The absorbance of 340 nm was measured by a microplate reader. The DNA damage repair in HCT116 cells was detected as reported [52]. Briefly, The HCT116 cells were co-transfected with 2 mg pCBASce or empty pcDNA vector, and either 4 mg pHPRT-DR-GFP plasmid. GFP expression in cells was analyzed using FACS at 48 h.

2.14. In vitro DNA double-strand breaks (γ-H₂AX immunofluorescence analysis)

HCT116 cells were seeded in confocal dishes at a density of 1×10^5 cells per dish for 24 h. Next, cells in each confocal dish were incubated with 6 different groups: (1) PBS; (2) NIR (660 nm laser, 1W/cm², 5min); (3) Flash (F, 10 Gy); (4) TH + NIR + F; (5) TCH + NIR; and (6) TCH + NIR + F. The CB-839 concentration was 40 µg/mL. The PTT and FLASH were conducted 2 h after different treatments. Then, the cells were fixed

by 4% paraformaldehyde for 30 min, rinsed three times with PBS, treated with triton-X 100 for 10 min at room temperature to enhance cell permeabilization, and then rinsed three times with PBS again. The cells were exposed to a blocking buffer (1% BSA in PBS) for 1 h at room temperature, and incubated with γ-H$_2$AX antibody (dilution 1:500) overnight at 4 °C. The next day, the cells were washed three times with PBS to remove the excess antibody and incubated with goat anti-mouse IgG (dilution 1:1000) for 1 h at room temperature. Cell nuclei were stained by DAPI at room temperature. At last, the cells were imaged by confocal microscopy (Leica, Wetzlar, Germany).

2.15. Clonogenic survival assay

In the radiation therapy experiment, 500 cells were seeded in eight 6-well plates incubating at hypoxic condition for 24 h, then the cells were incubated with 6 groups (1) PBS; (2) NIR (660 nm laser, 1 W/cm^2, 5 min); (3) FLASH (F, 10 Gy); (4) TH + NIR + F; (5) TCH + NIR; and (6) TCH + NIR + F. The CB-839 concentration was 40 μg/mL. The PTT and FLASH were conducted 2 h after different treatments. To allow the formation of colonies, after radiation, the cells were then incubated for another 10 days without changing the media. To determine the clonogenic survival rate, cultures were first fixed with paraformaldehyde, and then stained with trypan blue. Colonies with greater than 50 cells were counted under the microscope, and the survival fractions (SF) were calculated using the formula SF = colonies counted/cells seeded.

2.16. In vivo imaging

Female BALB/c nude mice aged 5–6 weeks were purchased from Vital River Company (Beijing, China). Mice were subcutaneously injected with 5×10^6 HCT116 cells into the right flank. When tumors reached 100 mm^3, Balb/c mice received an intratumoral injection of 100 μL PBS containing TDs or TCH (with a TPE-BBT dose of 10 mg/kg). At various time points after the injection (i.e., 0, 1, 6, 12, and 24 h), mice were imaged using the IVIS system.

2.17. In vivo infrared thermography

To monitor the *in vivo* photothermal effect, TCH was intratumorally injected into the tumor-bearing mice, and then the tumors were exposed to 1 W/cm^2 NIR-laser irradiation for 5 min at 1 h post-injection. PBS injection was conducted as the control group. The infrared thermal images were captured by a Fotric 225 Thermal Camera.

2.18. In vivo antitumor study

Female BALB/c nude mice aged 6 weeks were purchased from Vital River Company (Beijing, China). Balb/c mice were subcutaneously injected with 5×10^6 HCT116 cells into the right flank. When the tumor volume grew to 200 mm^3 (specified as day 0 at this time), the mice were divided randomly into 6 different groups (each group included 5 mice): (1) PBS; (2) NIR (660 nm laser, 1W/cm^2, 5min); (3) FLASH (F, 10 Gy); (4) TH + NIR + F; (5) TCH + NIR; and (6) TCH + NIR + F. The CB-839 concentration was 10 mg/kg. PTT and FLASH treatment occurred on days 0 and 3. PTT is conducted three times a day, and FLASH therapy is performed after PTT treatment. Mice body weight and tumor volume in all groups were monitored every 3 days. A caliper was employed to measure the tumor length and tumor width and the tumor volume was calculated according to following formula. Tumor volume = $0.5 \times$ tumor length $\times$ tumor width^2. At the end of treatments, mice were sacrificed. Six main organs (heart, liver, spleen, lung, intestine and kidney) of all mice were harvested, washed with PBS, and fixed with paraformaldehyde for histology analysis. Livers and lungs were collected to analyze their malondialdehyde (MDA) and superoxide dismutase (SOD) levels using total superoxide dismutase assay kits and malondialdehyde assay kits (Nanjing Jiancheng Bioengineering

Institute). Their blood samples were collected to measure three important hepatic indicators (i.e., ALT: alanine aminotransferase, AST: aspartate aminotransferase, and ALP: alkaline phosphatase) and two indicators for kidney functions (i.e., BUN: blood urea nitrogen and CRE: creatinine). The samples were measured by using a blood biochemical autoanalyzer (7080, HITACHI, Japan). Additionally, the tumor tissues were weighed and fixed in 4% neutral buffered formalin, processed routinely into paraffin, and then sectioned at 4 μm. Then, the primary tumor sections were stained with HE and γ-H$_2$AX antibody and finally examined by using a fluorescence microscope (IX81, Olympus, Japan). For traditional radiotherapy (RT) experiments, Balb/c mice were subcutaneously injected with 5×10^6 HCT116 cells into the right flank. When the tumor volume grew to 200 mm^3 (specified as day 0 at this time), the mice were divided randomly into 3 different groups (each group included 5 mice): (1) PBS; (2) RT (10 Gy); (3) TCH + NIR + RT. The treatment methods and dosages are the same as above. Tumor volumes in all groups were monitored every 3 days. A caliper was employed to measure the tumor length and tumor width and the tumor volume was calculated according to following formula. Tumor volume = $0.5 \times$ tumor length $\times$ tumor width^2. At the end of treatments, mice were sacrificed. Three main organs (liver, lung, and intestine) of all mice were harvested, washed with PBS, and fixed with paraformaldehyde for histology analysis. Livers and lungs were collected to analyze MDA and SOD levels using total superoxide dismutase assay kits and malondialdehyde assay kits (Nanjing Jiancheng Bioengineering Institute).

2.19. Statistical analysis

Data analyses were conducted using the GraphPad Prism 5.0 software. Significance between every two groups was calculated by the student's t-test. *$P < 0.05$, **$P < 0.01$, ***$P < 0.001$.

3. Results and discussion

3.1. Preparation, characterization, and photothermal effect of TDs

Fig. 1A shows the Jablonski diagram to depict the typical photophysical process of a molecule upon photon absorption. The excited molecule can return to the ground state via radiative or non-radiative decay, with the latter mainly converting the harvested light into heat. Most organic NIR-II fluorophores used in biological systems possess a QY of less than 1%, indicating that they possess intrinsic photothermal effects. Our previous study reported a NIR-II fluorophore named TPE-BBT, whose aggregate possesses an ultrahigh QY of 2.1% in water. Its high QY endows superior performance for FL bioimaging. If TPE-BBT demonstrates a satisfactory photothermal effect, it could be an ideal platform for phototheranostics. Therefore, water-soluble TPE-BBT dots (TDs) were prepared using a polymeric matrix of DSPE-PEG$_{2000}$ (Fig. 1B). The prepared TDs show similar absorption spectra as that of TPE-BBT aggregates in aqueous solutions, indicating the successful loading of TPE-BBT inside the nanoparticles (Fig. 1C). Dynamic light scattering (DLS) measurements suggest that TDs show an average diameter of 95.1 nm (Fig. 1D). This result is consistent with the analysis by transmission electron microscopy (TEM), which also suggests that TDs are uniformly spherical in shape (Fig. 1E). The photothermal effect of TDs was explored using a NIR laser (660 nm) as the excitation source. Fig. 1F and G demonstrate that increasing the TPE-BBT concentration in TDs and raising the NIR-laser power result in a quicker rise and a higher steady-state solution temperature. In addition, like many photothermal agents featuring MMFND, TPE-BBT boasts superior photostability, as the maximum elevated temperature triggered by the NPs demonstrates negligible changes after 5 cycles of photothermal tests (Fig. 1H). The photothermal conversion efficiency of TDs is calculated to be 16.97% based on the state-state temperature and cooling rate (Fig. S1 in the supporting information). This value is comparable with other commercial organic photothermal agents like ICG (~15%) [39,53]. Coupled
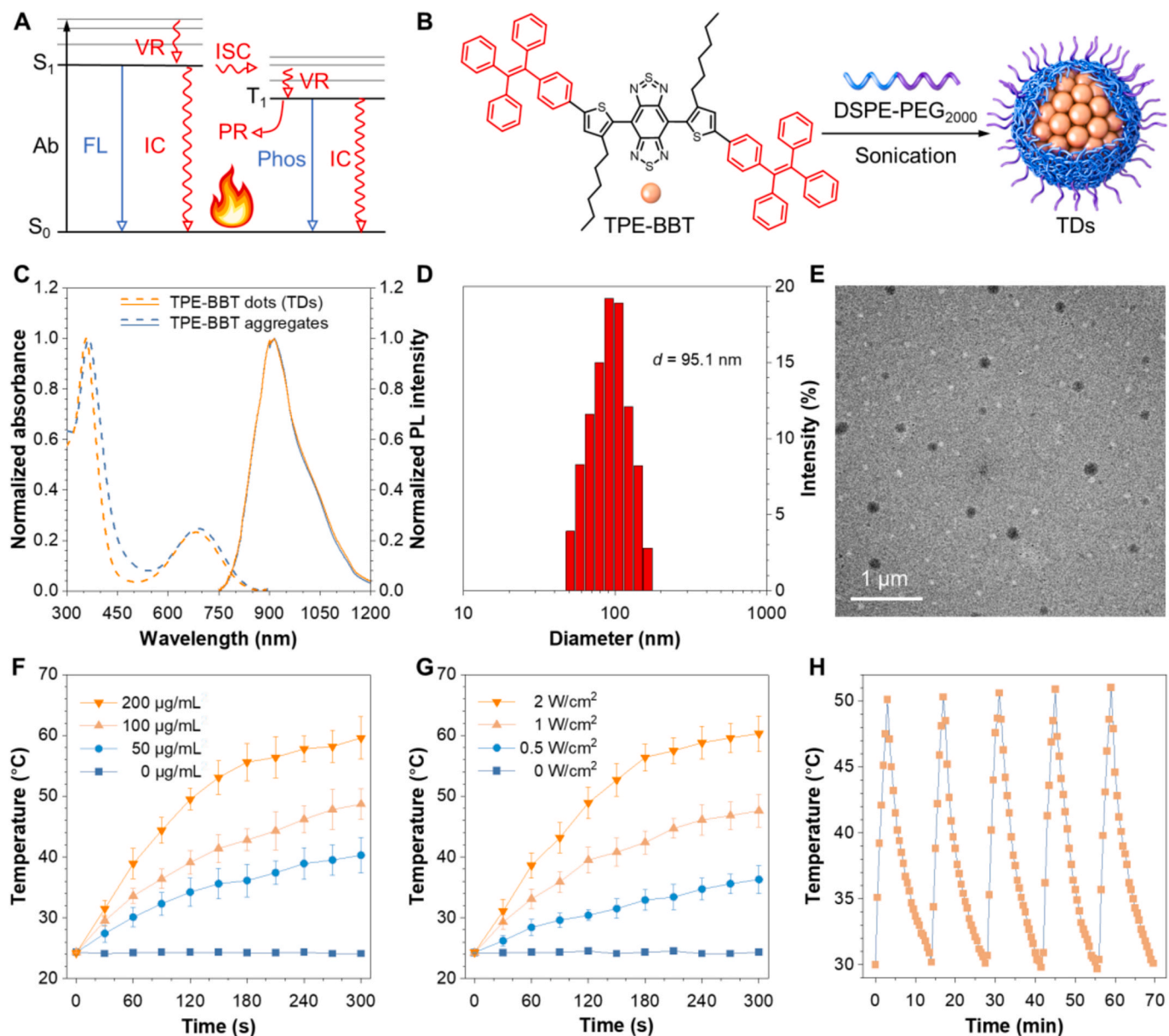
Fig. 1. Preparation and characterization of TPE-BBT dots (TDs). (A) Jablonski diagram of organic molecules showing the competition between radiative (blue color) and non-radiative (red color) processes. Ab: absorption; VR: vibrational relaxation; ISC: intersystem crossing; PR: photochemical reaction; IC: internal conversion; FL: fluorescence; Phos: phosphorescence. (B) Chemical structure of TPE-BBT and the preparation of TDs using DSPE-PEG$_{2000}$ as the surfactant. (C) Absorption and FL spectra of TDs in aqueous solution and TPE-BBT aggregates formed in a THF/water mixture with a water fraction of 99%. [TPE-BBT] = 10 μg/mL. (D) Size distribution of TDs in water. (E) TEM image of TDs. (F) The photothermal effect of TDs loaded with different contents of TPE-BBT in water under 660 nm laser irradiation with a power density of 1 W/cm². The data represent means ± SD; n = 3. (G) The photothermal effect of TDs loaded with 100 μg/mL of TPE-BBT in water under laser irradiation (660 nm) with different power densities. The data represent means ± SD; n = 3. (H) Thermostability of TDs loaded with 100 μg/mL of TPE-BBT in water during five cycles of heating–cooling processes.

with its much better photostability, TPE-BBT is an excellent candidate for PTT applications.

3.2. Theoretical calculation on the non-radiative process

TPE-BBT is a fluorophore showing the AIE property and photothermal effect. This motivates us to investigate how heat is generated upon laser irradiation. AIE is a unique photophysical phenomenon observed in some molecules showing weak emission in dilute solutions but significantly enhanced emission in the aggregate and solid states [54,55]. The mechanism behind this phenomenon is generalized as the restriction of intramolecular motion (RIM), which typically includes intramolecular rotation and vibration restriction [56,57]. Molecular

motions of AIE-active molecules typically require ample spatial area. Therefore, the close contact of a fluorophore with its surrounding neighbors in aggregates will decrease the free space and restrict these molecular motions. Our previous results indicate that TPE-BBT shows an ultrahigh QY due to the strong RIM effect in the crystalline state. However, TDs still demonstrate satisfactory photothermal effect, which indicates that non-radiative decay pathways are not entirely blocked. To gain more insights into this phenomenon, we compared its molecular motion behaviors under different conditions, including gas phase, aggregate phase, and crystalline phase through theoretical calculations (Fig. S2). Here, the aggregate model was simulated through molecular dynamics of TPE-BBT aggregates in aqueous environment, and the crystalline phase was extracted from its single-crystal structure. In

addition, we excluded the DSPE-PEG$_{2000}$ model in the calculation because TDs and TPE-BBT aggregates show similar photophysical properties (Fig. 1C). This implies that the surfactant alter little the behaviors of aggregated molecules.

Reorganization energy (λ) refers to the energy difference between the optimized ground-state and excited-state geometries, and can illustrate the strength and detailed behaviors of molecular motions after photoexcitation. Accordingly, the λ of TPE-BBT in its gas, crystalline, and aggregate phases were calculated and compared using the time-dependent density functional theory method (Fig. 2A–C). Considering the different environments between the surface and the core parts, the λ of both exposed and embedded TPE-BBT in aggregates was calculated. The decreased λ value in the crystalline phase (1747 cm^{-1}) compared to

the gas phase (2317 cm^{-1}) suggests that the aggregation process mainly influences the molecular motions at the low-frequency region (0–300 cm^{-1}), which refers to typical twisting molecular motions (Fig. 2A). When TPE-BBT is embedded in aggregates, its twisting motions are evidently inhibited (Fig. 2B). However, compared to the crystalline phase, the λ value in the low-frequency region is larger, mainly because of a less compact environment and a weaker RIM effect in aggregates. Fig. 2C illustrates the λ distribution of TPE-BBT exposed on the aggregate surface. Compared to the embedded TPE-BBT, the exposed TPE-BBT exhibits much enhanced twisting molecular motions, and the total λ value of the exposed TPE-BBT is comparable to that of TPE-BBT in the gas phase. By analyzing the molecular motion modes in the low-frequency region (Fig. S3), it is evident that the tetraphenylethylene
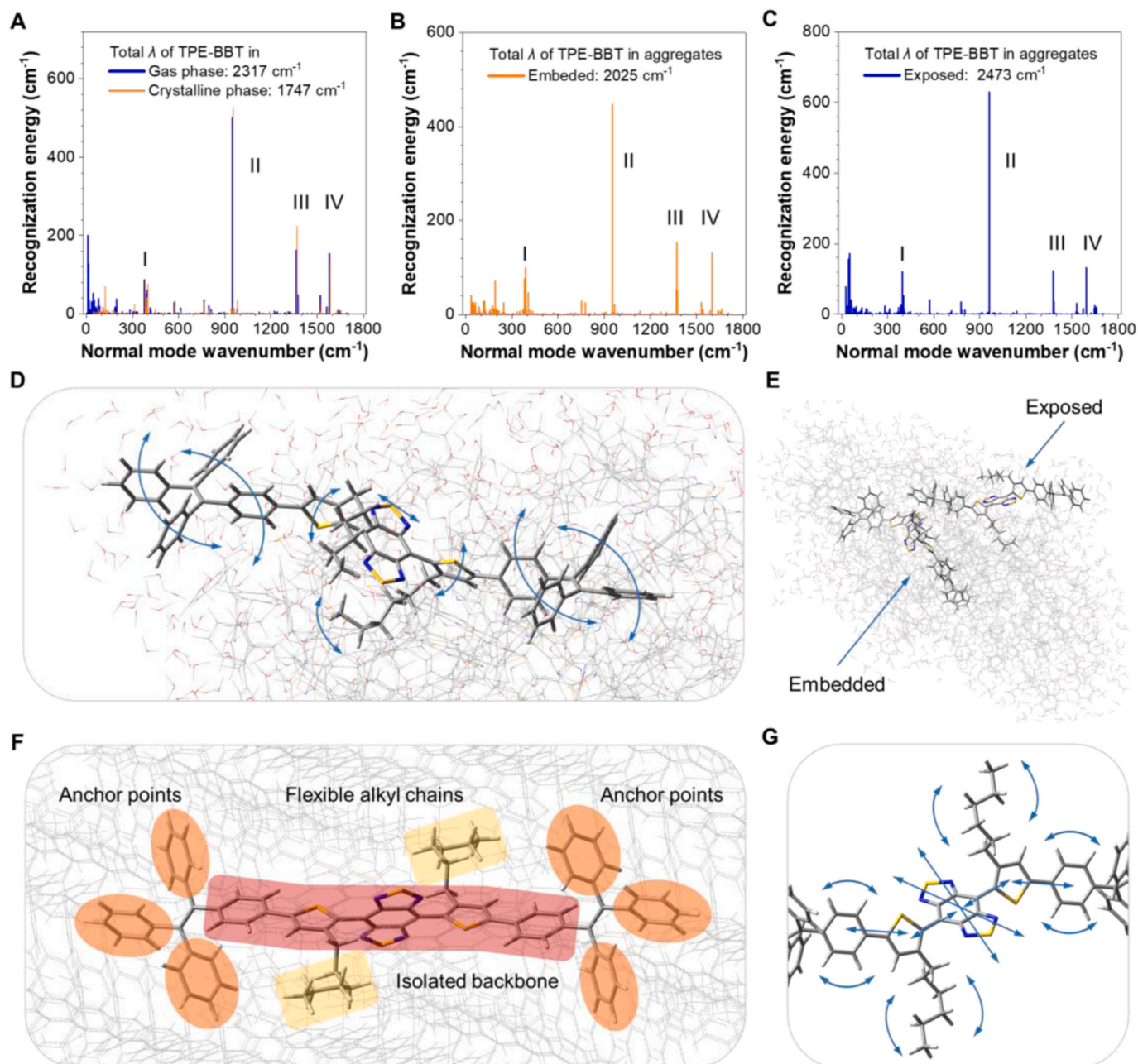

Fig. 2. Reorganization analysis and molecular motion modes of TPE-BBT in different environments. (A–C) Plots of reorganization energy (λ) versus normal mode wavenumber of TPE-BBT in (A) gas and crystalline phases, (B) surface part of the simulated aggregate (exposed TPE-BBT), and (C) core part of the simulated aggregate (embedded TPE-BBT). (D) Identified low-frequency molecular motion modes of exposed TPE-BBT in simulated aggregates. (E) Schematic illustration of two different kinds of TPE-BBT in the aggregate phase. (F) Spatial conformation characteristics of embedded TPE-BBT using the crystalline phase as the model. (G) Identified high-frequency molecular motion modes of embedded TPE-BBT using the crystalline phase as the model.

(TPE) units of TPE-BBT undergoes intense twisting motion due to the insufficient intermolecular interactions from the surrounding organic molecules in the surface environment (Fig. 2D). There is ample free space for the twisting motions of the exposed TPE-BBT. This finding suggests that TPE-BBT aggregates contain two distinct types of molecules. The TPE-BBT molecules on the aggregate surface behave like the isolated TPE-BBT, while the embedded TPE-BBT molecules are similar to crystalline TPE-BBT (Fig. 2E). The vigorous motions of the former efficiently dissipate the excited energy through non-radiative decay pathways to give rise to the photothermal effect. However, the fact that TPE-BBT exhibits much-enhanced FL when forming aggregates implies a high population of embedded TPE-BBT in aggregates. Therefore, we continued to investigate the molecular motions of embedded TPE-BBT.

The spatial sensitive low-frequency motions suggest that the photothermal effect in the aggregate state should be closely related to these motions without being efficiently restricted. Although the conformations of TPE-BBT in different phases differ significantly, all calculations exhibit similar motion modes in the high-frequency region ($>300\ \mathrm{cm}^{-1}$), implying that these molecular motions remain unaffected even after aggregation. To provide a detailed analysis, normal modes larger than $300\ \mathrm{cm}^{-1}$ are divided into four main regions (marked I–IV in Fig. 2A–C) and investigated. The representative motion modes of TPE-BBT in gas, crystalline, and embedded aggregate phases are shown in Figs. S4–S6. For clarity, we used the crystalline phase as the model to depict the molecular structures and motions of embedded TPE-BBT in the following content (Fig. 2F–G). Region I (wavenumber between 370 and $420\ \mathrm{cm}^{-1}$) contains several motion modes. The analysis of representative molecular motion modes in this region reveals that the outermost benzene rings of TPE remain relatively static, acting as six anchor points upon aggregation (A–C in Figs. S4–S6). Apart from molecular rotors, the conjugated backbone, which contains the BBT core, two thiophene bridges, and two linked phenyl rings, exhibits vivid vibration and stretching. The alkyl chains attached on the thiophene groups also undergo swing motions. Region II, which covers a wavenumber range of $950–955\ \mathrm{cm}^{-1}$, accounts for the largest λ of molecular motion mode (D in Figs. S4–S6). The stretching of the BBT core becomes dominant in Region II accompanied with backbone vibration and alkyl chain swing. Region III and IV (E and F in Figs. S4–S6) suggest that the stretching motions of the BBT core and the whole backbone vibration are dominant in all states. As identified in Fig. 2F, the bulky TPE units strongly interact with the surrounding fluorophores, and their motions will be significantly restricted as anchor points. However, the TPE units also isolate the conjugated backbone (highlighted in red zone in Fig. 2F), and the lack of intermolecular interactions will allow spatially insensitive molecular motions of the whole backbone. Concurrently, since the alkyl chains are flexible, their swing motions are also spatially insensitive (yellow zone in Fig. 2F). The detailed motion modes of embedded TPE-BBT are illustrated in Fig. 2G, including the BBT core stretching, the backbone vibration and stretching, and the alkyl chain swing. The results indicate that the spatially insensitive motions are still active upon aggregation, which become the main motion modes to contribute to the non-radiative decay of embedded TPE-BBT. To sum up, both exposed and embedded TPE-BBT in aggregates show vivid unrestricted molecular motions, which ensure the mild photothermal effect of TDs for practical applications.

3.3. Preparation and characterization of TCH

Based on the photothermal effect of TPE-BBT and its brilliant fluorescence properties, we incorporated it into a controllable drug release system. NIR light-responsive hydrogels show great potential for controlled drug release due to the non-invasiveness and adjustability of optical stimuli [58]. Agarose is a water-soluble linear polysaccharide extracted from seaweed, and it has shown promising features in fields ranging from environmental engineering to medicine [59]. Low-melting-point agarose melts at about 60 °C and undergoes a phase

transition to a gel state at physiological body temperature [60]. During hyperthermia, agarose undergoes reversible hydrolysis and softening, resulting in controllable drug permeation from the matrix into the surrounding environment. Thus, excited TDs in agarose can control the drug release of CB-839, evoke a synergistic mPTT for advanced therapy, and allow *in vivo* materials tracking. Due to the hydrophilicity of agarose, we first prepared CB-839 liposomes (CLs) to disperse the small-molecule drugs in the agarose solution homogeneously. As shown in Fig. 3A, the CLs absorb similar as CB-839 in aqueous medium. TEM image and DLS spectrum show the uniform spherical structure of CLs with a mean diameter of 97.8 nm (Fig. 3B–C). The prepared CLs demonstrate satisfactory cancer cell internalization (Fig. S7). Fig. 3D shows that the dipalmitoylphosphatidylcholine (DPPC) cholesterol liposomes exhibit an enhanced drug release under NIR laser-induced hyperthermia, which benefits the effectiveness on the tumor site. CLs and TDs show good stability as their diameters undergo a negligible change at 4 °C for 1 week (Fig. S8A). Next, we mixed CLs and TDs into an agarose solution at 60 °C. The solution was then cooled to room temperature to prepare a TDs and CLs co-loaded hydrogel (TCH). The image of scanning electron microscope (SEM) in Fig. 3E reveals the complex three-dimensional layered structure of TCH. Rheology measurement indicates the viscosity reduction at increasing temperature under laser irradiation, indicative of a lower crosslinking density (Fig. 3F). The temperature elevation and the release profile of CB-839 *in vitro* from TCH were then conducted. The TCH hydrogel was placed in a culture dish and allowed to stand for a while. The infrared thermal images of TCH were captured to record the temperature rise after the NIR-laser irradiation. As shown in Fig. 3G, the TCH temperature increases dramatically from 15.1 °C to 47.2 °C after irradiation for 5 min, and the hydrogel gradually softens to solution form after irradiation. The controlled release of CB-839 from TCH is depicted in Fig. 3H. The concentration of CB-839 increases significantly under irradiation, while the concentration without irradiation remains unchanged. Moreover, over one week without NIR irradiation, the leakage of CB-839 from TCH is less than 1%, as shown in Fig. S8B. These results suggest that TCH is a promising candidate for NIR-laser responsive drug delivery system.

3.4. In vitro antitumor therapy

Next, the antitumor effect of TCH was evaluated *in vitro* using HCT116 cells. We first investigated whether the TCH strategy can controllably inhibit GLS and the DNA repair process. The expression profiles of GLS in HCT116 cells at different conditions (when naming the groups, F refers to the FLASH process and TH refers to agarose gel loaded only with TDs) were analyzed with the Western blot. The results confirm that CLs can inhibit the GLS expression (Fig. S9). Glutamine metabolism is crucial for synthesizing GSH, which is the most abundant endogenous antioxidant that protects cells and tissues from oxidative stress induced by radiation therapy [23]. As shown in Fig. 4A, CLs efficiently downregulate the GSH level in HCT116 cells, while TCH alone has no significant impact. However, the NIR-laser irradiation of TCH leads to GSH inhibition, demonstrating that TCH can achieve controlled drug release for pharmaceutical effects. The DNA damage repair assay using pHPRT-DR-GFP indicates that CLs can inhibit the HR repair pathway of HCT116 cells (Fig. 4B). The NIR-laser can also release CB-839 for HR pathway inhibition. Moreover, the photothermal effect of TCH strengthens the inhibition effect due to the DNA damage effect of PTT. Thus, the NIR-laser responsive TCH can effectively induce DNA damage in cancer cells, which helps sensitize the consequential FLASH radiotherapy. Fig. 4C presents the results of the clonogenic survival assay in cancer cells. The introduction of the mPTT effect can efficiently boost the therapeutic effect, and the cytotoxicity depends on the TPE-BBT concentration. The TCH + NIR + F group exhibits the most pronounced inhibition of cancer cell growth to demonstrate a powerful synergistic effect. We further verified whether this synergistic effect is related to DNA damage by analyzing the phosphorylated histone H_2AX
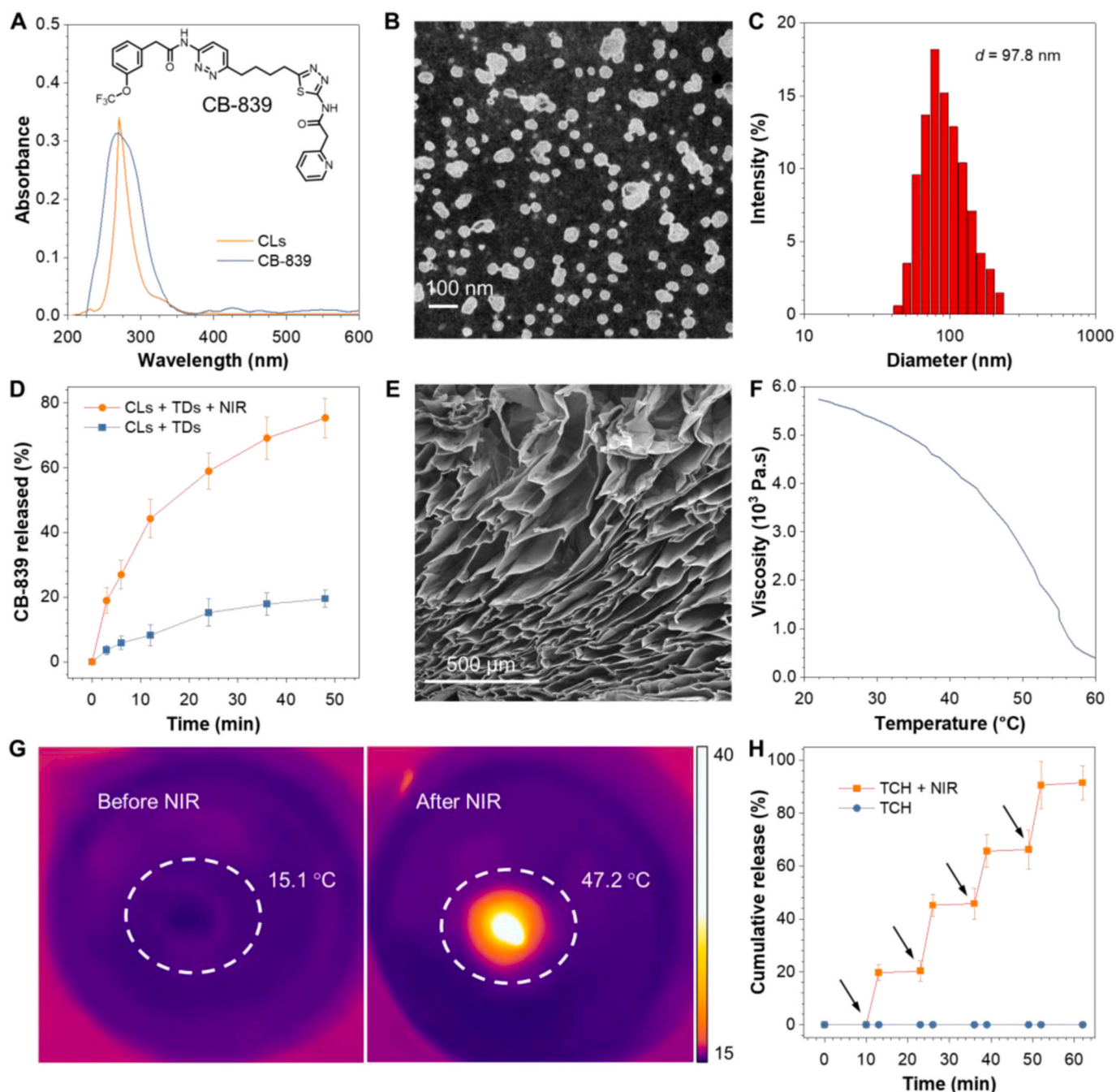
Fig. 3. Preparation and characterization of CB-839 liposomes (CLs) and TDs/CLs co-loaded hydrogel (TCH). (A) Chemical structure of CB-839 and absorption spectra of CB-839 (in PBS) and CLs (in PBS). The concentration of CB-839 is 40 μg/mL (B) TEM image of CLs. (C) Size distribution of CLs in aqueous solution. (D) *In vitro* CB-839 release profile from CLs with or without NIR-laser irradiation (660 nm, 1 W/cm², 3 min). (E) SEM image of TCH. (F) Rheological curve of TCH. (G) Infrared thermal images of TCH before and after NIR-laser irradiation (660 nm, 1 W/cm², 5 min). (H) The *in vitro* CB-839 release profile from TCH with or without NIR-laser irradiation (660 nm, 1 W/cm², 3 min at each time point indicated by the arrow).

(γ-H₂AX) (Fig. 4D). The γ-H₂AX immunofluorescence analysis demonstrates that the TCH + NIR + F group shows the most severe DNA damage. All these results prove that TCH can enhance the effect of FLASH by increasing the DNA damage.

3.5. In vivo antitumor therapy

The intriguing *in vitro* therapeutic efficacy of TCH stimulates us to investigate its *in vivo* antitumor phototheranostics. BALB/c nude mice were used for establishing subcutaneous tumor models using HCT116 cells. First, we tested whether the TCH could be used for *in vivo* tracking

of materials. Fig. S10 shows a clear FL signal from TCH under a *in vivo* IVIS imaging system. On the other hand, the biodistribution of TCH can be studied in detail through *ex vivo* fluorescence images (Fig. S11). *In vivo* photothermal experiments were then conducted on tumor-bearing mice. As shown in Fig. 5A, the photothermal images demonstrate that the temperature of the tumor tissue increases from 37.8 °C to 46.8 °C upon NIR irradiation. However, the tumor tissue without TCH only shows a negligible temperature increase (Fig. 5B and Fig. S12). We then investigated the antitumor effects of TCH. Fig. 5C represents the schematic illustration of the tumor treatment. The mice were treated with TCH injection followed by PTT and FLASH on days 0 and 3. The mice
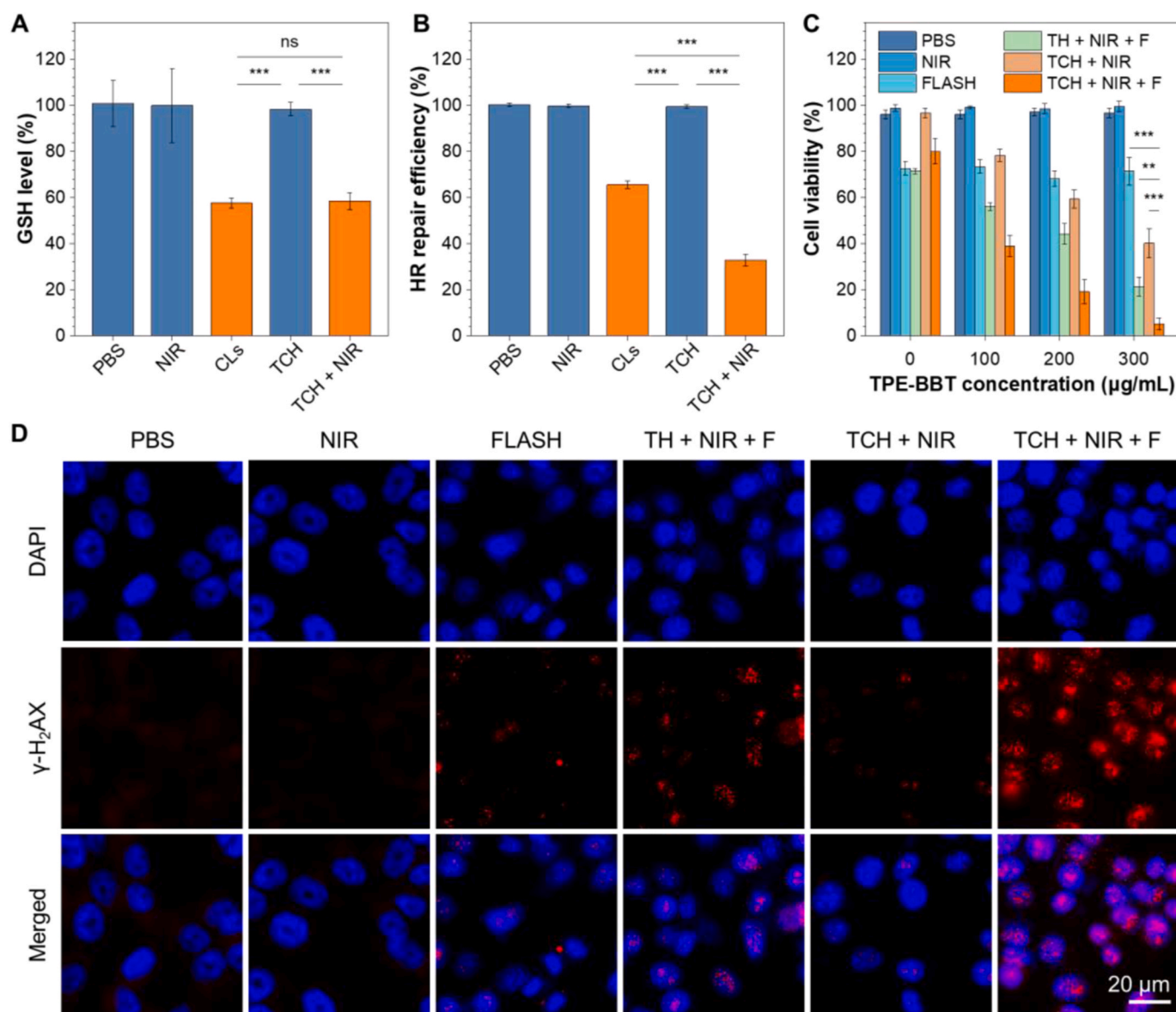
Fig. 4. *In vitro* mechanism research and antitumor therapy in HCT116 cells. (A) Intracellular detection of GSH content in HCT116 cells incubated at different conditions. ***$P < 0.001$; the data represent means ± SD; n = 3. (B) Intracellular detection of DNA damage repair in HCT116 cells incubated at different conditions. ***$P < 0.001$; the data represent means ± SD; n = 3. (C) Cell viability of HCT116 cells assessed by the chlorogenic survival assay at various incubation conditions. **$P < 0.01$; ***$P < 0.001$; the data represent means ± SD; n = 3. (D) *In vitro* analysis of DNA double-strand breaks in HCT116 cells using γ-H$_2$AX immunofluorescence analysis (λ_{ex} = 590 nm, λ_{em} = 617 nm).

tumor volume and body weight in all groups were then monitored every 3 days. As depicted in Fig. 5D–F, the mice treated with TCH + NIR + F exhibit a significantly stronger antitumor effect than the other groups. Furthermore, there was no observable tumor recurrence. In contrast, while other treatments can suppress the tumor growth, recurrence cannot be prevented, indicating an unsatisfactory treatment outcome and prognosis. The primary tumor sections after different treatments were analyzed using H&E staining (Fig. S13a). Compared to the control and other treatment groups, the tumor cell density in the TCH + NIR + F group decreases significantly, demonstrating the most potent tumor-killing effect. The tumor sections were further analyzed using γ-H$_2$AX immunofluorescence (Fig. S13b). The TCH + NIR + F group demonstrates the strongest FL signal, suggesting that the severe DNA damage ensures the outstanding antitumor effect. Additionally, the body weight of mice in every group shows no significant alteration, implying the biosafety of the designed strategy (Fig. 5G).

Due to the biosafety of the therapeutic agents, the potential systemic

toxicity of TCH + NIR + F was further evaluated in detail. Fig. 6A shows no noticeable organ damage or inflammatory lesions in the H&E-stained slices of major organs after the anticancer treatment. Compared to the PBS group, the blood biochemistry parameters of hepatic and renal function markers in the TCH + NIR + F groups appear to have no statistically significant difference (Fig. S14). This indicates no obvious systemic side effects of the TCH-based FLASH radiotherapy. We then assessed the therapeutic effect of conventional radiotherapy (RT) combined with TCH (Fig. S15). The results reveal that the synergistic effect of RT combined with NIR-laser irradiated TCH is also promising. However, further systemic toxicity studies highlight the potential biosafety concerns. We evaluated and compared the systemic toxicity of RT and FLASH combined with TCH under NIR-laser irradiation. Fig. 6B shows obvious organ damage in the TCH + NIR + RT group, especially with severe intestinal damage. To further prove the protection effect of the combined FLASH radiotherapy, we conducted the biochemical assessment of the liver and lung tissues by investigating the superoxide
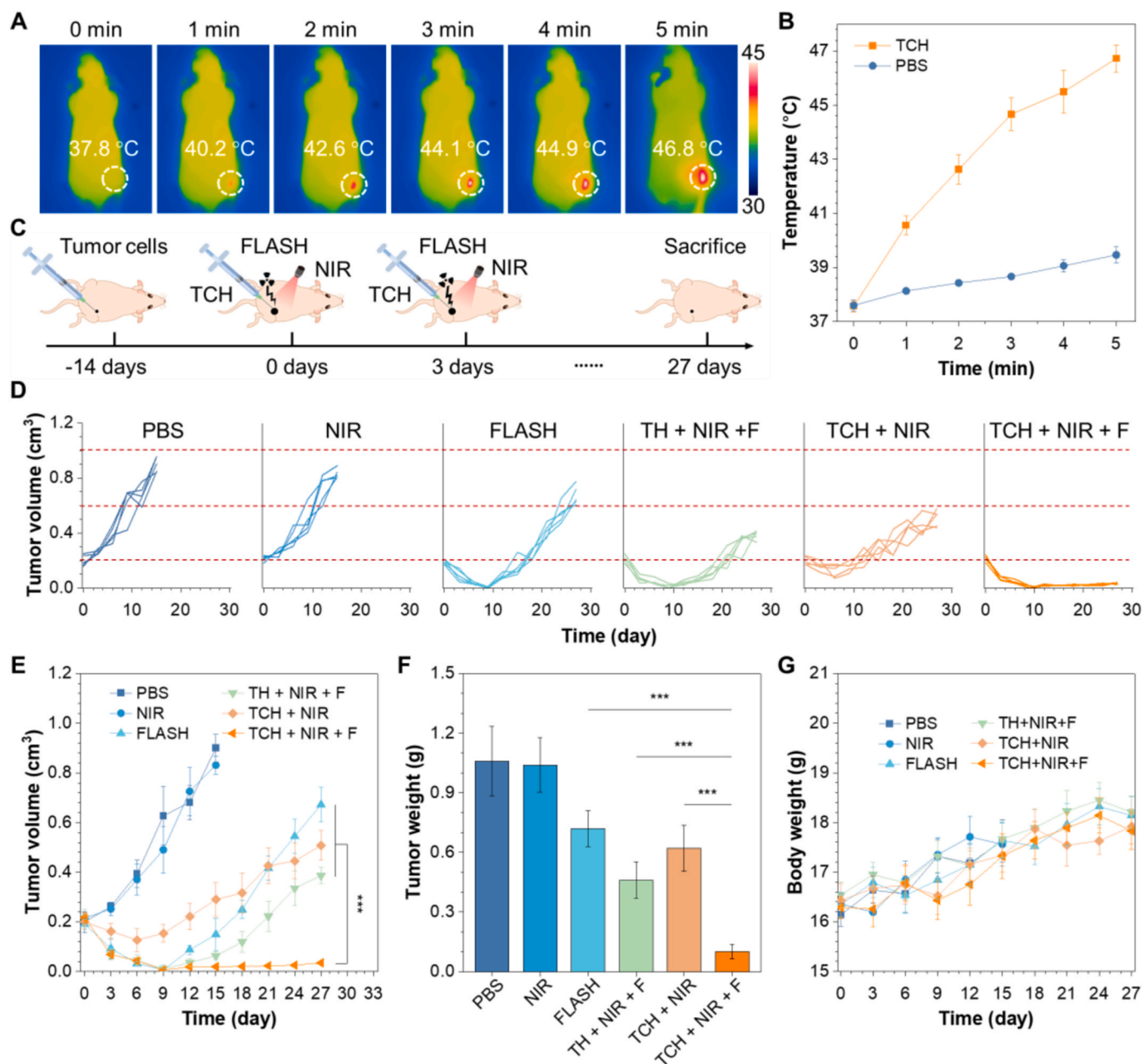
Fig. 5. *In vivo* **antitumor therapy using TCH in HCT116 tumor-bearing mice.** (A) Infrared thermal images of tumor-bearing mice under NIR-laser irradiation (660 nm, 1 W/cm^2) for 5 min after intratumoral injection of TCH (100 μL at a CB-839 dose of 10 mg/kg). (B) The temperature change of the mice irradiated with NIR laser. (C) Schematic illustration of the tumor treatment. (D) Individual tumor volume curves and (E) average tumor volume curves after various treatments. ***P < 0.001; the data represent means ± SD; n = 5. (F) Body weight change of mice subjected to various treatments during the antitumor therapy. (G) Evaluation of the tumor weight after the antitumor therapy. ***P < 0.001; the data represent means ± SD; n = 5.

dismutase (SOD) and 3,4-methylenedioxyamphetamine (MDA) levels. SODs are enzymes that convert superoxide radicals into molecular oxygen and hydrogen peroxide, serving as the first-line defense antioxidant. MDA is a stable end-product of lipid peroxidation and can be used to measure the lipid peroxidation level. Both SOD and MDA indicate levels of damage caused by ionizing radiation [61]. Fig. 6C–D show that the TCH + NIR + F group does not significantly affect SOD activities in the liver and lung when compared to the control group. However, the SOD activities noticeably decrease in the TCH + NIR + RT group. Fig. 6E–F examine MDA levels in the lung and liver. The results show a sharp increase in MDA levels due to the TCH + NIR + RT treatment. In contrast, there is no apparent difference in MDA levels between the TCH + NIR + F group and the normal group. The biochemical assessment of

liver and lung tissues supports the H&E staining results, demonstrating significantly higher biotoxicity in the TCH + NIR + RT group. These results confirm that combining FLASH radiotherapy with mPTT and CB-839 boasts excellent biocompatibility and biosafety.

According to the *in vitro* and *in vivo* biological evaluations, we have successfully developed a FLASH combined photothermal and chemotherapy for novel recurrence-resistant radiotherapy without adverse side effects. Compared with existing technologies for enhanced FLASH, our strategy offers unique advantages. TPE-BBT, the key component of our newly designed nanoplatform, operates in the NIR window. While phototherapy is commonly used for combined antitumor therapy, many of them work in a short wavelength range (e.g., white light irradiation) [62]. NIR excitation enables superior tissue penetration depth, thus
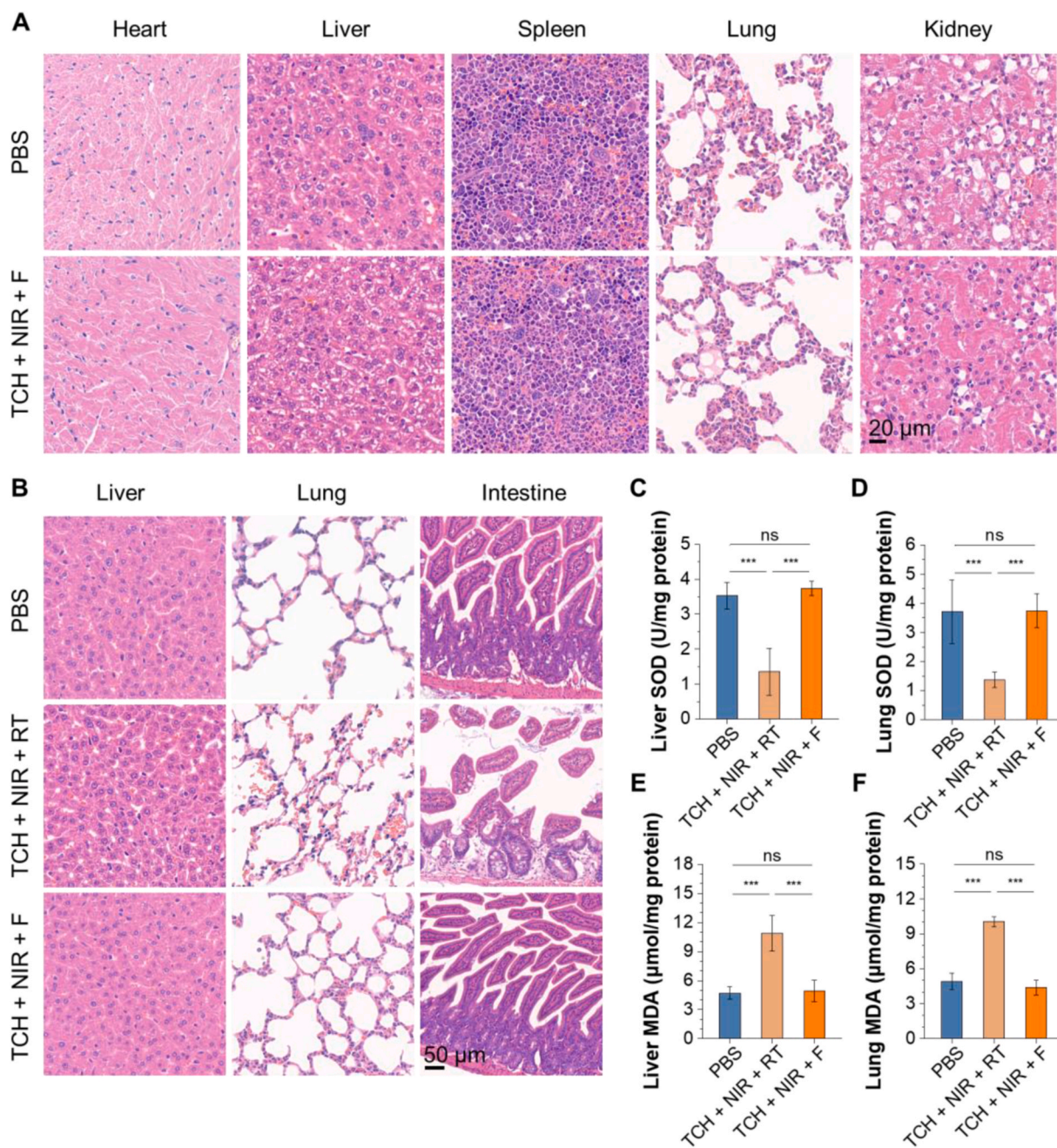
Fig. 6. Evaluation of the systematic toxicity. (A) Histological H&E staining analysis of major organs after PBS treatment and TCH + NIR + F. (B) Histological H&E staining analysis of major organs after PBS treatment, TCH + NIR + F, and TCH + NIR + RT. (C–F) Biochemical assessment for the liver and lung tissues of the mice after different treatments. Biomarkers include malondialdehyde (MDA) and superoxide dismutase (SOD). ***$P < 0.001$; the data represent means ± SD; n = 3.

offering better clinical translation potential. Importantly, in addition to the mPTT effect, TPE-BBT also provides bright fluorescence in the NIR window, ensuring efficient bioimaging and phototheranostics.

By utilizing the unique photophysical properties of TPE-BBT, we can enable mPTT and controllable drug release simultaneously. The efficient administration of small-molecule drugs can significantly enhance the antitumor effect. Using the controllable localized injectable hydrogel, we can easily achieve effective accumulation of the small-molecule drug CB-839 and the photothermal agent TPE-BBT in tumor tissues. Currently, various researchers have developed controllable drug delivery systems for combined radiotherapy [62,63]. However, their tumor-targeting effects are still limited due to the reticuloendothelial system barrier.

In tumor tissues, the TCH strategy effectively hinders DNA repair

processes and prevents tumor recurrence after FLASH radiotherapy. Despite numerous existing strategies for combined radiotherapy, there is insufficient focus on tumor recurrence and metastasis post-radiotherapy [63,64]. In our research, TCH inhibits DNA repair via two distinct mechanisms, significantly reducing the possibility of tumor recurrence after FLASH treatment. Our innovative photothermal nanoplatform offers valuable insights into current FLASH technology.

Our study still has several limitations, which suggests potential future directions. First, although the 660-nm excitation of TPE-BBT is in the NIR range, the NIR-II window with a wavelength longer than 1000 nm offers better penetration. In the future, we aim to discover new NIR-II excitable organic dyes with satisfactory fluorescence and photothermal effects for antitumor applications, which is highly desired but still challenging. Additionally, while CB-839 and mPTT influence the

DNA repair process via two distinct mechanisms, other factors, like cancer stem cells, can also induce tumor recurrence and metastasis [62]. Fortunately, the TCH platform is highly versatile and can load different therapeutic agents. Therefore, we will continue to explore combined therapy for better tumor treatment and prognosis outcomes.

4. Conclusion

In this work, the pioneering radiosensitizer TCH successfully overcame the tumor recurrence in FLASH technology, indicating new possibilities for next-generation radiotherapy. We utilized a combined strategy to inhibit the self-protective DDRs during FLASH radiotherapy by simultaneously targeting two mechanisms. The first approach disrupts glutamine metabolism using CB-839, while the second approach induces DNA damage through mPTT. Using TCH, we can control the release of CB-839 and conduct mPTT simultaneously to induce irreparable DNA damage upon NIR-laser exposure. As a result, FLASH radiotherapy can achieve enhanced radiation-induced cell death and show a superior antitumor effect without any tumor recurrence. Notably, the proposed FLASH combined therapy exhibits minimal toxicity to major tissues, indicating excellent biosafety while maintaining therapeutic efficacy.

Here, TPE-BBT with balanced photothermal effect and photoluminescence plays a central role in the recurrence-resistant FLASH therapy and materials tracking. Most NIR-II fluorophores have low QYs (<1%) to lead to significant energy loss as heat. TPE-BBT is a NIR-II fluorophore with an ultrahigh QY of about 2%, and it concurrently shows satisfactory photothermal generation in nanoparticles. Theoretical calculations decipher the unrestricted molecular motions in bright organic fluorophores as a source of photothermy. These findings provide new insights into the photothermal behavior of organic NIR-II fluorophores and demonstrate their potential as advanced phototheranostic agents.

Ethics approval and consent to participate

The animal experiments were carried out according to the protocol approved by the Ministry of Health in People's Republic of China and were approved by the Administrative Committee on Animal Research of Wuhan University (approval number: ZN2023107).

Ethics statements

The animal experiments were carried out according to the protocol approved by the Ministry of Health in People's Republic of China and were approved by the Experimental Animal Welfare Ethics Committee of Wuhan University.

CRediT authorship contribution statement

Hanchen Shen: Writing – original draft, Methodology, Conceptualization. **Hongbin Wang:** Methodology, Conceptualization. **Jianlan Mo:** Methodology, Conceptualization. **Jianyu Zhang:** Software, Methodology. **Changhuo Xu:** Methodology. **Feiyi Sun:** Methodology. **Xinwen Ou:** Software. **Xinyan Zhu:** Methodology. **Lidong Du:** Methodology. **Huaqiang Ju:** Methodology. **Ruquan Ye:** Investigation. **Guangfu Shi:** Methodology. **Ryan T.K. Kwok:** Resources. **Jacky W.Y. Lam:** Writing – review & editing, Resources. **Jianwei Sun:** Resources. **Tianfu Zhang:** Supervision, Conceptualization. **Shipeng Ning:** Resources, Methodology. **Ben Zhong Tang:** Supervision, Resources.

Declaration of competing interest

The authors declare that they have no known competing financial interests or personal relationships that could have appeared to influence the work reported in this paper.

Appendix A. Supplementary data

Supplementary data to this article can be found online at https://doi.org/10.1016/j.bioactmat.2024.03.024.

References

[1] L. Galluzzi, M.J. Aryankalayil, C.N. Coleman, S.C. Formenti, Emerging evidence for adapting radiotherapy to immunotherapy, Nat. Rev. Clin. Oncol. 20 (8) (2023) 543–557.

[2] H. Chen, Z. Han, Q. Luo, Y. Wang, Q. Li, L. Zhou, H. Zuo, Radiotherapy modulates tumor cell fate decisions: a review, Radiat. Oncol. 17 (1) (2022) 196.

[3] B. Lin, F. Gao, Y. Yang, D. Wu, Y. Zhang, G. Feng, T. Dai, X. Du, FLASH radiotherapy: history and future, Front. Oncol. 11 (2021) 644400.

[4] S.G. Park, Y.C. Ahn, D. Oh, J.M. Noh, S.G. Ju, D. Kwon, K. Jo, K. Chung, E. Chung, W. Lee, S. Park, Early clinical outcomes of helical tomotherapy/intensity-modulated proton therapy combination in nasopharynx cancer, Cancer Sci. 110 (9) (2019) 2867–2874.

[5] A.A. Friedl, K.M. Prise, K.T. Butterworth, P. Montay-Gruel, V. Favaudon, Radiobiology of the FLASH effect, Med. Phys. 49 (3) (2022) 1993–2013.

[6] V. Favaudon, L. Caplier, V. Monceau, F. Pouzoulet, M. Sayarath, C. Fouillade, M.-F. Poupon, I. Brito, P. Hupé, J. Bourhis, J. Hall, J.-J. Fontaine, M.-C. Vozenin, Ultrahigh dose-rate FLASH irradiation increases the differential response between normal and tumor tissue in mice, Sci. Transl. Med. 6 (245) (2014) 245ra93.

[7] U.A. Weber, E. Scifoni, M. Durante, FLASH radiotherapy with carbon ion beams, Med. Phys. 49 (3) (2022) 1974–1992.

[8] P. Montay-Gruel, M.M. Acharya, K. Petersson, L. Alikhani, C. Yakkala, B.D. Allen, J. Ollivier, B. Petit, P.G. Jorge, A.R. Syage, T.A. Nguyen, A.A.D. Baddour, C. Lu, P. Singh, R. Moeckli, F. Bochud, J.F. Germond, P. Froidevaux, C. Bailat, J. Bourhis, M.C. Vozenin, C.L. Limoli, Long-term neurocognitive benefits of FLASH radiotherapy driven by reduced reactive oxygen species, Proc. Natl. Acad. Sci. U.S.A. 116 (22) (2019) 10943–10951.

[9] E. Hageman, P.P. Che, M. Dahele, B.J. Slotman, P. Sminia, Radiobiological aspects of FLASH radiotherapy, Biomolecules 12 (10) (2022) 1376.

[10] T. Suwa, M. Kobayashi, J.M. Nam, H. Harada, Tumor microenvironment and radioresistance, Exp. Mol. Med. 53 (6) (2021) 1029–1035.

[11] S. de Mey, I. Dufait, M. De Ridder, Radioresistance of human cancers: clinical implications of genetic expression signatures, Front. Oncol. 11 (2021) 761901.

[12] J. Gu, N. Mu, B. Jia, Q. Guo, L. Pan, M. Zhu, W. Zhang, K. Zhang, W. Li, M. Li, L. Wei, X. Xue, Y. Zhang, W. Zhang, Targeting radiation-tolerant persister cells as a strategy for inhibiting radioresistance and recurrence in glioblastoma, Neuro Oncol. 24 (7) (2022) 1056–1070.

[13] L.Y. Li, Y.D. Guan, X.S. Chen, J.M. Yang, Y. Cheng, DNA repair pathways in cancer therapy and resistance, Front. Pharmacol. 11 (2020) 629266.

[14] R.X. Huang, P.K. Zhou, DNA damage response signaling pathways and targets for radiotherapy sensitization in cancer, Signal Transduct. Targeted Ther. 5 (1) (2020) 60.

[15] M. Wang, S. Chen, D. Ao, Targeting DNA repair pathway in cancer: mechanisms and clinical application, MedComm 2 (4) (2021) 654–691.

[16] S. Fu, Z. Li, L. Xiao, W. Hu, L. Zhang, B. Xie, Q. Zhou, J. He, Y. Qiu, M. Wen, Y. Peng, J. Gao, R. Tan, Y. Deng, L. Weng, L.Q. Sun, Glutamine synthetase promotes radiation resistance via facilitating nucleotide metabolism and subsequent DNA damage repair, Cell Rep. 28 (5) (2019) 1136–1143.

[17] H. Jin, S. Wang, E.A. Zaal, C. Wang, H. Wu, A. Bosma, F. Jochems, N. Isima, G. Jin, C. Lieftink, R. Beijersbergen, C.R. Berkers, W. Qin, R. Bernards, A powerful drug combination strategy targeting glutamine addiction for the treatment of human liver cancer, Elife 9 (2020) e56749.

[18] R.S. Alden, M.Z. Kamran, B.A. Bashjawish, B.A. Simone, Glutamine metabolism and radiosensitivity: beyond the Warburg effect, Front. Oncol. 12 (2022) 1070514.

[19] T.Q. Tran, M.B. Ishak Gabra, X.H. Lowman, Y. Yang, M.A. Reid, M. Pan, T. R. O'Connor, M. Kong, Glutamine deficiency induces DNA alkylation damage and sensitizes cancer cells to alkylating agents through inhibition of ALKBH enzymes, PLoS Biol. 15 (11) (2017) e2002810.

[20] N. Goel, M.E. Foxall, C.B. Scalise, J.A. Wall, R.C. Arend, Strategies in overcoming homologous recombination proficiency and PARP inhibitor resistance, Mol. Cancer Therapeut. 20 (9) (2021) 1542–1549.

[21] Y. Zhao, X. Feng, Y. Chen, J.E. Selfridge, S. Gorityala, Z. Du, J.M. Wang, Y. Hao, G. Cioffi, R.A. Conlon, J.S. Barnholtz-Sloan, J. Saltzman, S.S. Krishnamurthi, S. Vinayak, M. Veigl, Y. Xu, D.L. Bajor, S.D. Markowitz, N.J. Meropol, J.R. Eads, Z. Wang, 5-Fluorouracil enhances the antitumor activity of the glutaminase inhibitor CB-839 against PIK3CA-mutant colorectal cancers, Cancer Res. 80 (21) (2020) 4815–4827.

[22] C.A. Wicker, B.G. Hunt, S. Krishnan, K. Aziz, S. Parajuli, S. Palackdharry, W. R. Elaban, T.M. Wise-Draper, G.B. Mills, S.E. Waltz, V. Takiar, Glutaminase inhibition with telaglenastat (CB-839) improves treatment response in combination with ionizing radiation in head and neck squamous cell carcinoma models, Cancer Lett. 502 (2021) 180–188.

[23] G. Boysen, A. Jamshidi-Parsian, M.A. Davis, E.R. Siegel, C.M. Simecka, R.A. Kore, R.P.M. Dings, R.J. Griffin, Glutaminase inhibitor CB-839 increases radiation sensitivity of lung tumor cells and human lung tumor xenografts in mice, Int. J. Radiat. Biol. 95 (4) (2019) 436–442.

[24] J.H. Lee, Injectable hydrogels delivering therapeutic agents for disease treatment and tissue engineering, Biomater. Res. 22 (2018) 27.

[25] M. Qiu, D. Wang, W. Liang, L. Liu, Y. Zhang, X. Chen, D.K. Sang, C. Xing, Z. Li, B. Dong, F. Xing, D. Fan, S. Bao, H. Zhang, Y. Cao, Novel concept of the smart NIR-light-controlled drug release of black phosphorus nanostructure for cancer therapy, Proc. Natl. Acad. Sci. U.S.A. 115 (3) (2018) 501–506.

[26] C. Zhu, D. Huo, Q. Chen, J. Xue, S. Shen, Y. Xia, A eutectic mixture of natural fatty acids can serve as the gating material for near-infrared-triggered drug release, Adv. Mater. 29 (40) (2017) 1703702.

[27] C. Liu, X. Guo, C. Ruan, H. Hu, B.P. Jiang, H. Liang, X.C. Shen, An injectable thermosensitive photothermal-network hydrogel for near-infrared-triggered drug delivery and synergistic photothermal-chemotherapy, Acta Biomater. 96 (2019) 281–294.

[28] S. Li, Q. Deng, Y. Zhang, X. Li, G. Wen, X. Cui, Y. Wan, Y. Huang, J. Chen, Z. Liu, L. Wang, C.S. Lee, Rational design of conjugated small molecules for superior photothermal theranostics in the NIR-II biowindow, Adv. Mater. 32 (33) (2020) e2001146.

[29] T. Zhang, J. Zhang, F.B. Wang, H. Cao, D. Zhu, X. Chen, C. Xu, X. Yang, W. Huang, Z. Wang, J. Wang, Z. He, Z. Zheng, J.W.Y. Lam, B.Z. Tang, Mitochondria-targeting phototheranostics by aggregation-induced NIR-II emission luminogens: modulating intramolecular motion by electron acceptor engineering for multi-modal synergistic therapy, Adv. Funct. Mater. 32 (16) (2022) 2110526.

[30] D. Wang, M.L. Kuzma, X. Tan, T.C. He, C. Dong, Z. Liu, J. Yang, Phototherapy and optical waveguides for the treatment of infection, Adv. Drug Deliv. Rev. 179 (2021) 114036.

[31] X. Wu, Y. Jiang, N.J. Rommelfanger, F. Yang, Q. Zhou, R. Yin, J. Liu, S. Cai, W. Ren, A. Shin, K.S. Ong, K. Pu, G. Hong, Tether-free photothermal deep-brain stimulation in freely behaving mice via wide-field illumination in the near-infrared-II window, Nat. Biomed. Eng. 6 (6) (2022) 754–770.

[32] F. Sun, H. Shen, Q. Yang, Z. Yuan, Y. Chen, W. Guo, Y. Wang, L. Yang, Z. Bai, Q. Liu, M. Jiang, J.W.Y. Lam, J. Sun, R. Ye, R.T.K. Kwok, B.Z. Tang, Dual behavior regulation: tether-free deep-brain stimulation by photothermal and upconversion hybrid nanoparticles, Adv. Mater. 35 (21) (2023) e2210018.

[33] Y. Zhang, D. Yang, J. Nie, J. Dai, H. Wu, J.C. Zheng, F. Zhang, Y. Fang, Transcranial nongenetic neuromodulation via bioinspired vesicle-enabled precise NIR-II optical stimulation, Adv. Mater. 35 (3) (2023) e2208601.

[34] Y. Duan, D. Hu, B. Guo, Q. Shi, M. Wu, S. Xu, Kenry, X. Liu, J. Jiang, Z. Sheng, H. Zheng, B. Liu, Nanostructural control enables optimized photoacoustic–fluorescence–magnetic resonance multimodal imaging and photothermal therapy of brain tumor, Adv. Funct. Mater. 30 (1) (2019) 1907077.

[35] C. Li, Y. Cheng, D. Li, Q. An, W. Zhang, Y. Zhang, Y. Fu, Antitumor applications of photothermal agents and photothermal synergistic therapies, Int. J. Mol. Sci. 23 (14) (2022) 7909.

[36] G. Gao, X. Sun, G. Liang, Nanoagent-promoted mild-temperature photothermal therapy for cancer treatment, Adv. Funct. Mater. 31 (25) (2021) 2100738.

[37] Y. Yu, T. Wang, X. Meng, T. Jiang, X. Zhao, Chitosan thermosensitive hydrogel based on DNA damage repair inhibition and mild photothermal therapy for enhanced antitumor treatment, Biomacromolecules 24 (2023) 3755–3766.

[38] Y. Xiong, W. Wang, Q. Deng, Z. Zhang, Q. Wang, Z. Yong, C. Sun, X. Yang, Z. Li, Mild photothermal therapy boosts nanomedicine antitumor efficacy by disrupting DNA damage repair pathways and modulating tumor mechanics, Nano Today 49 (2023) 101767.

[39] C. Xu, R. Ye, H. Shen, J.W.Y. Lam, Z. Zhao, B. Zhong Tang, Molecular motion and nonradiative decay: towards efficient photothermal and photoacoustic systems, Angew. Chem. Int. Ed. 61 (30) (2022) e202204604.

[40] H. Shen, C. Xu, R. Ye, T.-M. Liu, J. Zhang, R.T.K. Kwok, J.W.Y. Lam, Z. Guo, J. Sun, B.Z. Tang, Water-soluble aggregation-induced emission luminogens with near-infrared emission for advanced photetheranostics, Small Sci 3 (2023) 2300052.

[41] Y. Liu, Y. Li, S. Koo, Y. Sun, Y. Liu, X. Liu, Y. Pan, Z. Zhang, M. Du, S. Lu, X. Qiao, J. Gao, X. Wang, Z. Deng, X. Meng, Y. Xiao, J.S. Kim, X. Hong, Versatile types of inorganic/organic NIR-IIa/IIb fluorophores: from strategic design toward molecular imaging and theranostics, Chem. Rev. 122 (2021) 209–268.

[42] H. Shen, F. Sun, X. Zhu, J. Zhang, X. Ou, J. Zhang, C. Xu, H.H.Y. Sung, I. D. Williams, S. Chen, R.T.K. Kwok, J.W.Y. Lam, J. Sun, F. Zhang, B.Z. Tang, Rational design of NIR-II AIEgens with ultrahigh quantum yields for photo- and chemiluminescence imaging, J. Am. Chem. Soc. 144 (33) (2022) 15391–15402.

[43] Y. Zhao, D.G. Truhlar, The M06 suite of density functionals for main group thermochemistry, thermochemical kinetics, noncovalent interactions, excited states, and transition elements: two new functionals and systematic testing of four M06-class functionals and 12 other functionals, Theor. Chem. Acc. 120 (1) (2008) 215–241.

[44] P.C. Hariharan, J.A. Pople, Accuracy of AH n equilibrium geometries by single determinant molecular orbital theory, Mol. Phys. 27 (1) (1974) 209–214.

[45] S. Grimme, J. Antony, S. Ehrlich, H. Krieg, A consistent and accurate ab initio parametrization of density functional dispersion correction (DFT-D) for the 94 elements H-Pu, J. Chem. Phys. 132 (15) (2010) 154104.

[46] E. Runge, E.K.U. Gross, Density-functional theory for time-dependent systems, Phys. Rev. Lett. 52 (12) (1984) 997–1000.

[47] M.J. Frisch, G.W. Trucks, H.B. Schlegel, G.E. Scuseria, M.A. Robb, J.R. Cheeseman, G. Scalmani, V. Barone, G.A. Petersson, H. Nakatsuji, X. Li, M. Caricato, A. V. Marenich, J. Bloino, B.G. Janesko, R. Gomperts, B. Mennucci, H.P. Hratchian, J. V. Ortiz, A.F. Izmaylov, J.L. SonnenbergWilliams, F. Ding, F. Lipparini, F. Egidi, J. Goings, B. Peng, A. Petrone, T. Henderson, D. Ranasinghe, V.G. Zakrzewski, J. Gao, N. Rega, G. Zheng, W. Liang, M. Hada, M. Ehara, K. Toyota, R. Fukuda, J. Hasegawa, M. Ishida, T. Nakajima, Y. Honda, O. Kitao, H. Nakai, T. Vreven, K. Throssell, J.A. Montgomery Jr., J.E. Peralta, F. Ogliaro, M.J. Bearpark, J. J. Heyd, E.N. Brothers, K.N. Kudin, V.N. Staroverov, T.A. Keith, R. Kobayashi, J. Normand, K. Raghavachari, A.P. Rendell, J.C. Burant, S.S. Iyengar, J. Tomasi, M. Cossi, J.M. Millam, M. Klene, C. Adamo, R. Cammi, J.W. Ochterski, R.L. Martin, K. Morokuma, O. Farkas, J.B. Foresman, D.J. Fox, Gaussian 16 Rev. C.01, Wallingford, CT, 2016.

[48] Z. Shuai, Q. Peng, Excited states structure and processes: understanding organic light-emitting diodes at the molecular level, Phys. Rep. 537 (4) (2014) 123–156.

[49] Z. Shuai, Q. Peng, Organic light-emitting diodes: theoretical understanding of highly efficient materials and development of computational methodology, Natl. Sci. Rev. 4 (2) (2016) 224–239.

[50] Z. Shuai, Thermal vibration correlation function formalism for molecular excited state decay rates, Chin. J. Chem. 38 (11) (2020) 1223–1232.

[51] D. Zhu, M. Lyu, Q. Huang, M. Suo, Y. Liu, W. Jiang, Y. Duo, K. Fan, Stellate plasmonic exosomes for penetrative targeting tumor NIR-II thermo-radiotherapy, ACS Appl. Mater. Interfaces 12 (33) (2020) 36928–36937.

[52] Y. Wang, B. Wei, D. Wang, J. Wu, J. Gao, H. Zhong, Y. Sun, Q. Xu, W. Liu, Y. Gu, W. Guo, DNA damage repair promotion in colonic epithelial cells by andrographolide downregulated cGAS−STING pathway activation and contributed to the relief of CPT-11-induced intestinal mucositis, Acta Pharm. Sin. B 12 (1) (2022) 262–273.

[53] S. Zeng, H. Gao, C. Li, S. Xing, Z. Xu, Q. Liu, G. Feng, D. Ding, Boosting photothermal theranostics via TICT and molecular motions for photohyperthermia therapy of muscle-invasive bladder cancer, Adv. Healthcare Mater. 10 (24) (2021) e2101063.

[54] H. Zhang, Z. Zhao, A.T. Turley, L. Wang, P.R. McGonigal, Y. Tu, Y. Li, Z. Wang, R.T. K. Kwok, J.W.Y. Lam, B.Z. Tang, Aggregate science: from structures to properties, Adv. Mater. 32 (2020) e2001457.

[55] M. Kang, Z. Zhang, N. Song, M. Li, P. Sun, X. Chen, D. Wang, B.Z. Tang, Aggregation-enhanced theranostics: AIE sparkles in biomedical field, Aggregate 1 (1) (2020) 80–106.

[56] J. Zhang, H. Zhang, J.W.Y. Lam, B.Z. Tang, Restriction of intramolecular motion (RIM): investigating AIE mechanism from experimental and theoretical studies, Chem. Res. Chin. Univ. 37 (1) (2021) 1–15.

[57] J. Yang, M. Fang, Z. Li, Organic luminescent materials: the concentration on aggregates from aggregation-induced emission, Aggregate 1 (1) (2020) 6–18.

[58] T. Zhang, Z. Liu, W. Tang, D. Zhu, M. Lyu, J.W.Y. Lam, Q. Huang, B.Z. Tang, Mitochondria-targeting Type I AIE photosensitizer combined with H2S therapy: uninterrupted hydroxyl radical generation for enhancing tumor therapy, Nano Today 46 (2022) 101620.

[59] M. Khodadadi Yazdi, A. Taghizadeh, M. Taghizadeh, F.J. Stadler, M. Farokhi, F. Mottaghitalab, P. Zarrintaj, J.D. Ramsey, F. Seidi, M.R. Saeb, M. Mozafari, Agarose-based biomaterials for advanced drug delivery, J. Contr. Release 326 (2020) 523–543.

[60] M. Hou, R. Yang, L. Zhang, L. Zhang, G. Liu, Z. Xu, Y. Kang, P. Xue, Injectable and natural humic acid/agarose hybrid hydrogel for localized light-driven photothermal ablation and chemotherapy of cancer, ACS Biomater. Sci. Eng. 4 (12) (2018) 4266–4277.

[61] X.D. Zhang, J. Zhang, J. Wang, J. Yang, J. Chen, X. Shen, J. Deng, D. Deng, W. Long, Y.M. Sun, C. Liu, M. Li, Highly catalytic nanodots with renal clearance for radiation protection, ACS Nano 10 (4) (2016) 4511–4519.

[62] M. Lyu, T. Zhang, Y. Li, J. Xiang, D. Zhu, L. Xia, B. Guo, Y. Xu, H. Yu, B. Tang, AIEgen-based nanotherapeutic strategy for enhanced FLASH irradiation to prevent tumour recurrence and avoid severe side effects, Chem. Eng. J. 473 (2023) 145179.

[63] Y. Wu, J. Qin, Y. Gu, G. Zhao, P. Xu, S. Lin, X. Cheng, L.W. Zhang, Y. Wang, Y. Wang, Radioresponsive delivery of toll-like receptor 7/8 agonist for tumor radioimmunotherapy enabled by core-cross-linked diselenide nanoparticles, ACS Nano 18 (4) (2024) 2800–2814.

[64] Y.C. Dong, L.M. Nieves, J.C. Hsu, A. Kumar, M. Bouché, U. Krishnan, K. J. Mossburg, D. Saxena, S. Uman, T. Kambayashi, J.A. Burdick, M.M. Kim, J. F. Dorsey, D.P. Cormode, Novel combination treatment for melanoma: FLASH radiotherapy and immunotherapy delivered by a radiopaque and radiation responsive hydrogel, Chem. Mater. 35 (22) (2023) 9542–9551.